Remote Sensing of Environment 181 (2016) 174–185

Contents lists available at ScienceDirect

Remote Sensing of Environment

journal homepage: www.elsevier.com/locate/rse

Assessing uncertainty and sensor biases in passive microwave data across High Mountain Asia

Taylor Smith *, Bodo Bookhagen

Institute of Earth and Environmental Sciences, Universität Potsdam, Germany

ARTICLE INFO

Article history:
Received 3 December 2015
Received in revised form 3 March 2016
Accepted 31 March 2016
Available online xxxx

Keywords:
Snow-Water Equivalent
Passive Microwave
SSMI/S
AMSR-E
AMSR2
GPM

ABSTRACT

Snowfall comprises a significant percentage of the annual water budget in High Mountain Asia (HMA), but snow-water equivalent (SWE) is poorly constrained due to lack of in-situ measurements and complex terrain that limits the efficacy of modeling and observations. Over the past few decades, SWE has been estimated with passive microwave (PM) sensors with generally good results in wide, flat, terrain, and lower reliability in densely forested, complex, or high-elevation areas.

In this study, we use raw swath data from five satellite sensors — the Special Sensor Microwave/Imager (SSMI) and Special Sensor Microwave Imager/Sounder (SSMIS) (1987–2015, F08, F11, F13, F17), Advanced Microwave Scanning Radiometer — Earth Observing System (AMSR-E, 2002–2011), AMSR2 (2012–2015), and the Global Precipitation Measurement (GPM, 2014–2015) — in order to understand the spatial and temporal structure of native sensor, topographic, and land cover biases in SWE estimates in HMA. We develop a thorough understanding of the uncertainties in our SWE estimates by examining the impacts of topographic parameters (aspect, relief, hillslope angle, and elevation), land cover, native sensor biases, and climate parameters (precipitation, temperature, and wind speed). HMA, with its high seasonality, large topographic gradients and low relief at high elevations provides an excellent context to examine a wide range of climatic, land-cover, and topographic settings to better constrain SWE uncertainties and potential sensor bias.

Using a multi-parameter regression, we compare long-term SWE variability to forest fraction, maximal multi-year snow depth, topographic parameters, and long-term average wind speed across both individual sensor time series and a merged multi-sensor dataset. In regions where forest cover is extensive, it is the strongest control on SWE variability. In those regions where forest density is low (<5%), maximal snow depth dominates the uncertainty signal. In our regression across HMA, we find that forest fraction is the strongest control on SWE variability (75.8%), followed by maximal multi-year snow depth (7.82%), 90th percentile 10-m wind speed of a 10-year December-January-February (DJF) time series (5.64%), 25th percentile DJF 10-m wind speed (5.44%), and hillslope angle (5.24%). Elevation, relief, and terrain aspect show very low influence on SWE variability (<1%). We find that the GPM sensor provides the most robust regression results, and can be reliably used to estimate SWE in our study region.

While forest cover and elevation have been integrated into many SWE algorithms, wind speed and long-term maximal snow depth have not. Our results show that wind redistribution of snow can have impacts on SWE, especially over large, flat, areas. Using our regression results, we have developed an understanding of sensor-specific SWE uncertainties and their spatial patterns. The uncertainty maps developed in this study provide a first-order approximation of SWE-estimate reliability for much of HMA, and imply that high-fidelity SWE estimates can be produced for many high-elevation areas.

1. Introduction

Tracking the accumulation and melt of snow is essential for weather forecasting, climate modeling, and water management applications. Estimates of snow depth (SD) and snow-water equivalent (SWE) provide additional information on the volume of water stored and released from snowpack, which is critical for managing flood risk, irrigation systems, and hydropower (Armstrong & Brodzik, 2002), (Tedesco & Narvekar, 2010). Several methods have been used to estimate SD and SWE over large areas, such as modeling based on snow covered area (SCA) and a conversion factor (Bookhagen & Burbank, 2010), (Immerzeel, Droogers, De Jong, & Bierkens, 2009), estimating melt volume by backward calculation of snow clearance dates (Molotch & Margulis, 2008; Guan et al., 2013), direct measurements of SWE with in-situ climate stations, and SWE estimation with passive microwave (PM) data (Chang, Foster, Hall, Rango, & Hartline, 1982; Chang, Foster,

* Corresponding author at: Institute of Earth and Environmental Sciences, Universität Potsdam, Potsdam-Golm 14476, Germany.
E-mail address: tasmith@uni-potsdam.de (T. Smith).

http://dx.doi.org/10.1016/j.rse.2016.03.037
0034-4257/

& Hall, 1987; Clifford, 2010; Daly et al., 2012; Pulliainen, 2006; Takala, Pulliainen, Metsämäki, & Koskinen, 2009; Takala et al., 2011; Tedesco, Derksen, Deems, & Foster, 2015). SWE estimation with PM data is the only method which can estimate SWE over large areas, across all terrain types, and provide high-temporal resolution SWE estimates based on empirical relationships. High temporal-resolution data is imperative for accurately guaging snowmelt and downstream runoff (Anderton, White, & Alvera, 2002; Dozier, Painter, Rittger, & Frew, 2008; Painter et al., 2009).

Beginning in 1978 with the Scanning Multichannel Microwave Radiometer (SMMR) system, PM data has been used to measure snow parameters (Knowles, Njoku, Armstrong, & Brodzik, 2002; Chang et al., 1982). PM data has several significant advantages over optical remote sensing data for the collection of snow data, including cloud penetration, night-time data collection, and high sensitivity to water content in snowpack. For many snow-covered regions, winter storms can drastically limit optical data collection due to cloud cover. The Special Sensor Microwave/Imager (SSMI) (Wentz, 2013), Special Sensor Microwave Imager/Sounder (SSMIS) (Sun & Weng, 2008), Advanced Microwave Scanning Radiometer — Earth Observing System (AMSR-E) (Ashcroft & Wentz, 2013), AMSR2 (Imaoka et al., 2010), and Global Precipitation Measurement (GPM) (GPM Science Team, 2014) sensors each collect data at several microwave spectra, and can be used for the evaluation of snowpack at daily or greater resolution.

Several algorithms have been developed to estimate SD and SWE from PM data (e.g., (Chang et al., 1987; Kelly, Chang, Tsang, & Foster, 2003; Pulliainen, 2006; Kelly, 2009; Tedesco & Narvekar, 2010; Takala et al., 2011). The majority of these algorithms exploit the difference between the brightness temperatures (Tb) at the ~18 and ~36 GHz channels. However, more recent algorithms, such as those proposed by (Kelly, 2009), also exploit the ~10, ~23, and ~89 GHz channels available on AMSR-E/2 and GPM, which can better resolve shallow snow conditions and are less sensitive to saturation of the PM signal at the ~18 GHz band (Derksen, 2008). Improvements on SWE estimation have also been made by tuning the original equations proposed by (Chang et al., 1987) to specific regional conditions (Mizukami & Perica, 2012), correcting for elevation (Savoie, Armstrong, Brodzik, & Wang, 2009), and by introducing a forest cover correction (Foster et al., 2005). While these methods have improved upon SWE estimation, they remain unreliable in complex topography (Tedesco et al., 2015).

Topographic relief can have strong impacts on sensed Tb values (Mätzler & Standley, 2000;Dozier & Warren, 1982). First, the path between the ground surface and the PM sensor is determined by the ground elevation, which can introduce a height-dependent bias (Savoie et al., 2009). Second, complex terrain can interact constructively, where the sensed Tb values are not only the PM radiation emitted by a flat surface, but the combination of interacting microwave signals from hillslopes which face each other. Third, topography can shadow parts of the satellite field of view, which preferentially samples those hillslopes which face the satellite. Last, land surface slope changes the relative look angle of the satellite, which can preferentially enhance or degrade the microwave signal from different areas of the same field of view, and modify the relative signal strengths of horizontally and vertically polarized Tb data (Dozier & Warren, 1982). In addition to topographic impacts, forest cover can significantly reduce the Tb difference term used by SWE algorithms (Chang, Foster, & Hall, 1996; Foster et al., 2005). This is due to the attenuation of microwave signals as they pass through dense vegetation, which can reduce SWE estimates by as much as 50% (Brown, 1996; Vander Jagt et al., 2013).

While studies have examined the reliability of SWE data from several satellite platforms (i.e. Imaoka et al., 2010; Armstrong & Brodzik, 2001; Armstrong & Brodzik, 2002; Brown, 1996; Chang et al., 1996; Dai, Che, & Ding, 2015; Foster et al., 2005; Langlois et al., 2011;Mizukami & Perica, 2012; Sun & Weng, 2008; Tedesco & Narvekar, 2010; Wang & Tedesco, 2007; Savoie et al., 2009; Dong, Walker, & Houser, 2005), few large-scale analyses of SWE have been undertaken in High Mountain Asia (HMA), and none have examined the impacts of long-term maximal snow depth and wind redistribution on SWE variability.

As HMA lacks an extensive and reliable ground-weather station network, particularly at elevations above 3000 m, we do not rely on in-situ data to compare our satellite-based SWE estimates to those of any snow-monitoring stations. Instead, we focus on understanding the utility and limitations of satellite-based PM data – especially those factors which may reduce the reliability of SWE estimates – by examining a multi-frequency time series of PM data across a range of topographic, land cover, and climate settings.

2. Materials and methods

In this study we use a multi-instrument time series of SSMI, SSMIS, AMSR-E, AMSR2, and GPM PM data from 2000–2015 in combination with topographic, land-cover, and climatic data.

2.1. Study area

Our study area encompasses a wide range of climatic seasonality, elevation, topographic relief and hillslope angles. It includes not only high relief and high complexity areas typical of many mountain ranges, but also large areas of low relief at high elevation (i.e., the Tibetan Plateau). Low but variable forest density across the study region, in combination with the range of topographic characteristics, allows us to examine a range of factors which impact SWE estimation with PM data. We randomly generated 5000 points within our study area, and removed those close to major bodies of water. From this subset, we choose 2500 sample points which cover a wide range of elevation, relief, slope, and aspect settings (Fig. 1).

2.2. Topographic, land cover, and climate data

The 2000 Shuttle Radar Topography Mission V4.1 (SRTM) Digital Elevation Model (DEM) (~90-m, void-filled) was leveraged to provide elevation, hillslope angle, aspect, and 5-km radius relief (Jarvis, Reuter, Nelson, Guevara, et al., 2008) (Fig. 1). We then apply an averaging filter over a 20-km radius to the hillslope, elevation, and relief surfaces to minimize spatial-resolution differences and PM location uncertainties when comparing between 90-m and ~25-km resolution data (Fig. 2A, B).

High Asia Reanalysis (HAR) (2000–2014) provides 10-km resolution land-surface temperature at 2-m heights (product t2) at both daily and 3-hourly temporal resolution over 98% of the study area for the period 2000 to 2014 (Maussion et al., 2014). For those points which fall outside of the 10-km HAR domain, we use the 30-km product instead. We use the hourly product to create average daily daytime and nighttime temperatures, as well as bi-daily deviation values from the long-term average monthly temperatures. In addition to the HAR temperature product, we leverage the 10-m surface wind speed dataset (product ws10) to assess the impact of high-wind areas on SWE variability (Fig. 2C). We treat the HAR wind product as a 'static' dataset in our analysis by using long-term statistics derived from the 14-year time series of wind speed data, such as the long-term December-January-February (DJF) median, 25th and 90th percentile wind speeds at each pixel. By using percentiles as proxies for long-term trends in the climate data, we can more accurately compare trends in wind speed with trends in SWE and SWE variability over the whole time series instead of on a daily or hourly basis.

TRMM product 3B42 V7 (1997–2014) provides daily rainfall estimates at $0.25° \times 0.25°$ resolution (Huffman et al., 2007). This data is used to isolate precipitation-free days and multi-day periods from the larger time series, with a sensed precipitation threshold of 0.1 mm/h.

Fractional forest cover is derived from MODIS MOD12Q1 yearly data (2001 − 2012), following the Boston University IGBP classification

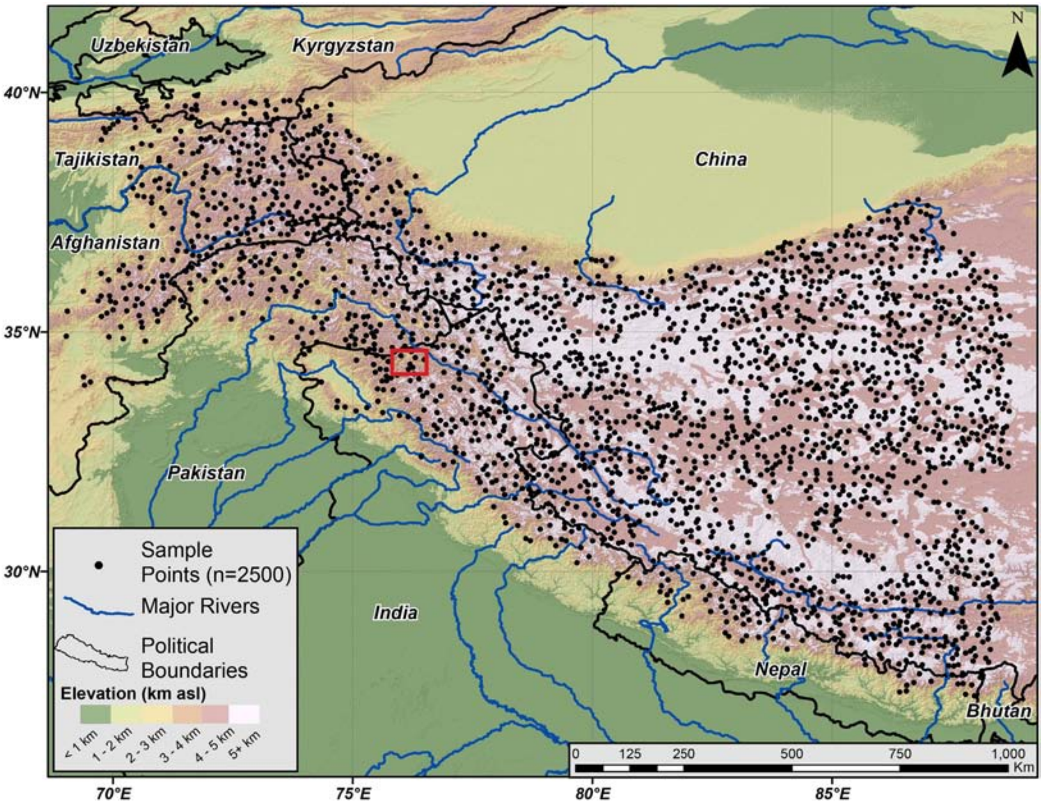

Fig. 1. Topographic map of High Mountain Asia (HMA) based on SRTM V4.1 data with political boundaries (black) and major rivers (blue). Black dots indicate randomly-generated sample points (n = 2500) encompassing a wide range of land cover, topographic, and climate regimes. Red box indicates extent of Fig. 3. For each sample point, we have extracted a multi-instrument time series of PM data, landscape characteristics (forest cover, hillslope angle, elevation, aspect, relief), and climate data (rainfall, temperature, wind speed). (For interpretation of the references to color in this figure legend, the reader is referred to the web version of this article.)

scheme (Hansen et al., 2003). Forest density is derived from MODIS MOD44B global forest density yearly data (2000–2010, (DiMiceli et al., 2011)). Both MOD12Q1 and MOD44B area averaged over a 20-km radius (Fig. 2D).

The AMSR EASEgrid SWE product (L3 v2, 2002–2011) provides SWE estimates at 0.25° × 0.25° resolution across our entire study area (Tedesco, Kelly, Foster, & Chang, 2004). The EASEgrid product at daily resolution is used to visually compare the SWE estimation of a large-scale gridded products with the results of our point-level SWE analyses. We also use the AMSR EASEgrid product to examine the distribution of snow depth throughout our study area. In our analysis of SWE uncertainty, we use the 9-year daily resolution time series of SWE measurements to derive 95th percentile SWE volume estimates for each grid cell. These estimates serve as proxies for tracking areas which see frequent deep snow cover.

To identify time periods which should nominally have constant SWE (i.e., no changes in SWE), we choose those periods where (1) the HAR temperature does not rise above 0 °C and (2) there is no sensed precipitation, as measured by TRMM. These periods are termed 'clear days' throughout this manuscript, and are used in Sections 3 and 4 to examine native inter- and intra-sensor variability.

2.3. Passive microwave data

In this study we acquired ungridded, raw, swath data for SSMI and SSMIS (F08, F11, F13, F17, 1987–2015, (Wentz, 2013; Sun & Weng, 2008)), AMSR-E (2002–2010, (Ashcroft & Wentz, 2013)), AMSR2 (2012–2015, (Imaoka et al., 2010)), and GPM (2014–2015, (GPM Science Team, 2014)) satellites. The characteristics of each satellite are listed in Table 1.

We examined the potential of the TRMM Microwave Imager (TMI) instrument to measure SWE, but found the results unreliable. In particular, the 36 V channel experienced highly variable Tb fluctuations, making SWE estimation with the TMI sensor problematic.

2.4. Swath processing

We examine the raw, orbital PM data at each satellite's respective native sensor resolution and do not resample the data to an equally-spaced or consistent grid. By maintaining native resolution, we are able to increase our data density by using multiple imperfectly-overlapping swaths (Fig. 3). Native resolution also improves direct, point-by-point comparisons between horizontally and vertically polarized data points by avoiding any data resampling. In this study, we use 30,865,102 individual data points across five satellites and 2500 random sample locations to examine long-term aggregate and inter-sensor differences in PM data. We also process a subset of 14,804,414 data points which occur on 'clear days', or days which do not see temperatures above 0°C and have no sensed precipitation.

To examine the swath data at 2500 randomly chosen point locations across the study area, we implement a search algorithm to find the closest data point within each individual swath (maximum distance 0.1°, approx. 10 km) throughout the entire measurement period of each satellite. To test the influence of the chosen search distance on Tb values at any given point, we have examined whole time series Tb means and standard deviations against the distance from the sampling center point (Fig. S1 in the Supplement). Across search distances, the means and standard deviations do not change appreciably, indicating that while there may be some changes in the variability signal we see within a subsetted dataset, these changes are due to the reduction in data density and not due to variability in the satellite field of view over time.

In this way, we develop a time series of Tb values at each point location at native instrument spatial resolution (Fig. 3). Using the time of each individual capture in conjunction with the latitude and longitude

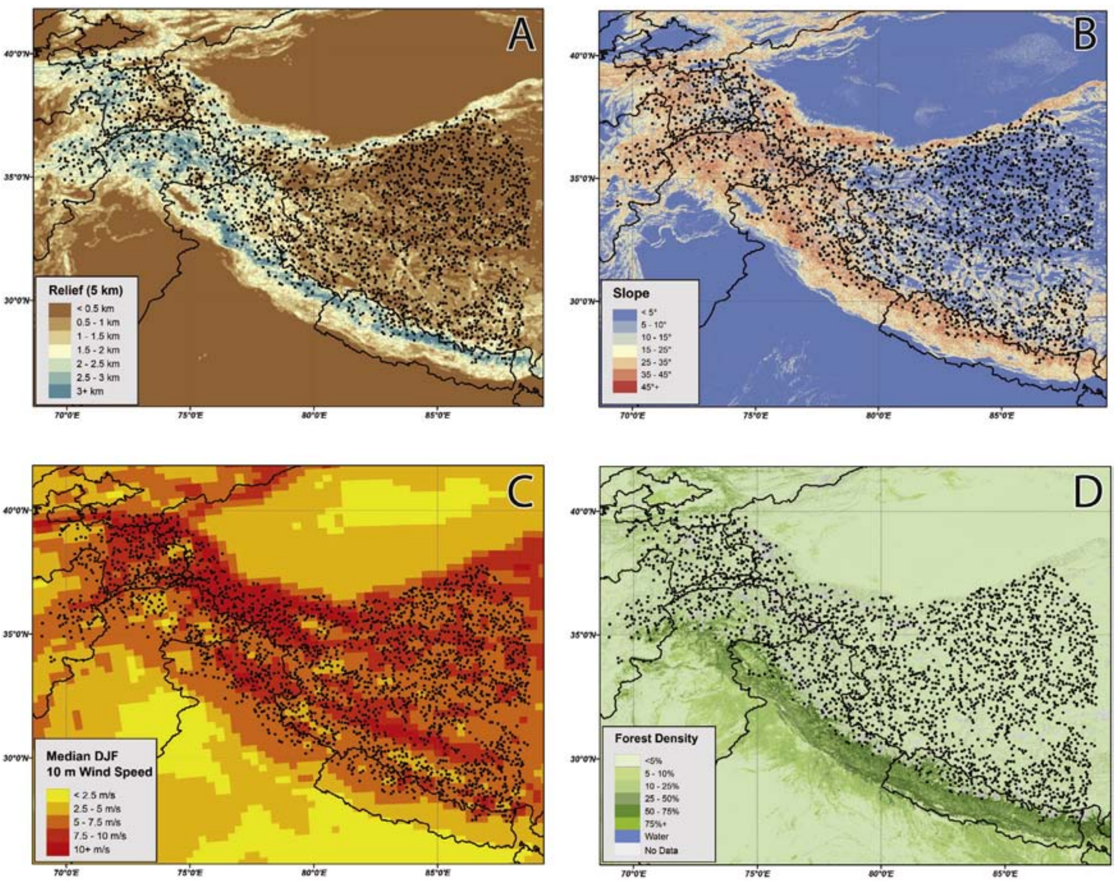

Fig. 2. Topographic and climatic characteristics of High Mountain Asia: (A) 5-km radius relief and (B) hillslope angle (degree), derived from SRTM V4.1 and averaged over a 20-km radius (Jarvis et al., 2008); (C) 14-year averaged December-January-February (DJF) median 10-m wind speed (m/s), derived from HAR (Maussion et al., 2014), and (D) forest density, derived from MOD44B (2000–2010, (DiMiceli et al., 2011)). Black dots indicate random sample locations (cf. Fig. 1).

of the point location, we derive the position of the sun relative to the horizon. In our analysis of SWE, we only use those points where the sun is below the horizon. While this method is more computationally expensive than using only the descending orbits of each satellite, it allows us to expand our dataset by including every data point which is captured at night, regardless of which orbit it falls in. It also allows us to examine intra-day differences in measured Tb through the daytime and nighttime subsets of the Tb time series.

Finally, we implement a correction to the SSMI/S data, as proposed by (Dai et al., 2015), to normalize the SSMI/S data received from the multiple satellites (F08, F11, F13, F17). In this way, we ensure that each satellite dataset is as internally consistent as possible. We assume that the inter-calibration between AMSR-E and AMSR2 is of high quality, and thus do not perform any additional inter-calibration for the AMSR sensors.

2.5. SWE estimation

Although several SWE estimation algorithms have been proposed (e.g., Chang et al., 1987; Kelly et al., 2003; Pulliainen, 2006; Kelly, 2009; Takala et al., 2011; Mizukami & Perica, 2012; Savoie et al., 2009; Tong, Dery, Jackson, & Derksen, 2010), this study chooses to use only

Table 1
Characteristics of PM sensors used, with native channel frequencies, spatial resolutions, processing algorithms, orbit frequencies, and satellite angular properties.

Satellite	Temporal coverage	Channels (GHz)	Spatial resolution (km^2)	Processing level/algorithm
SSMI	Aug 1987–Apr 2009 (22 years)	19.35, 22, 36, 85	69 × 43, 60 × 40, 37 × 28, 16 × 14	FCDR V07
SSMI/S	Jan 2008–Apr 2015 (7 years)	19.35, 22, 36, 92	69 × 43, 60 × 40, 37 × 28, 37 × 28	FCDR V07
AMSR-E	May 2002–Oct 2011 (9 years)	6.93, 10.65, 18.7, 23.8, 36.5, 89	75 × 43, 51 × 29, 27 × 16, 27 × 16, 14 × 8, 6 × 4	L1B
AMSR2	Jul 2012–Sep 2015 (3 years)	6.93, 7.3, 10.65, 18.7, 23.8, 36.5, 89	62 × 35, 62 × 35, 42 × 24, 22 × 14, 19 × 11, 12 × 7, 5 × 3	L1R
GPM	Feb 2014–Jul 2015 (1.5 years)	10.65, 18.7, 23.8, 36.5, 89, 166, 183.31	32.2 × 19.4, 18.3 × 11.2, 15 × 9.2, 14.4 × 8.6, 7.3 × 4.4, 7.1 × 4.4, 7.2 × 4.4	L1B

Satellite	Number of orbits (descending/ascending)	Average observations per month	Earth incidence angle (°)	Scan angle range (°)
SSMI	176,460/176,460	1411	53.1	±51.2
SSMI/S	41,896/41,896	901	53.1	±71.6
AMSR-E	49,083/49,079	868	55	±61
AMSR2	16,623/16,623	874	55	±61
GPM	3919/3919	435	52.8	±70

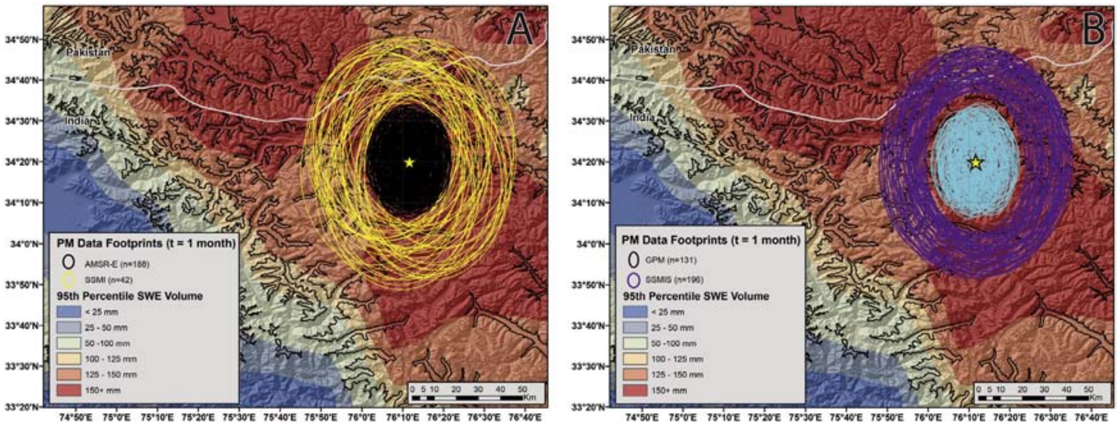

Fig. 3. Characteristic example of raw PM data points and their ellipsoidal geographic extent in NW India (cf. Fig. 1). (A) One month of data from the SSMI (yellow, n = 42) and AMSR-E (black, n = 188) satellites; (B) SSMIS (purple, n = 196) and GPM (turquoise, n = 131). AMSR2 not shown, as the footprint size and density is comparable to AMSR-E. We show 9-year 95th percentile SWE volume from the AMSR EASEgrid as a background image to elucidate the 10-fold southwest-to-northeast SWE gradient in this area. Gray lines indicate international borders, black lines show the 4-km elevation contour. (For interpretation of the references to color in this figure legend, the reader is referred to the web version of this article.)

two of these to examine SD and SWE. The first method is based on the Chang equation:

$$SD[cm] = 1.59[cm/K] * (Tb_{18v} - Tb_{36v})[K] \tag{1}$$

This equation has seen wide use across the SSMI/S and AMSR-E platforms. To our knowledge, the Chang equation has never been used with GPM data to estimate SWE. However, due to the similar spectral ranges carried onboard AMSR-E/2 and GPM, we assume that the modified Chang equation, as proposed by (Armstrong & Brodzik, 2001), will work equally well for the GPM platform.

We also use a more complex algorithm – as initially developed for the AMSR-E satellite (Kelly et al., 2003; Kelly, 2009; Tedesco & Narvekar, 2010) – that includes a measure of forest cover and density. Both forest fraction and forest density have been shown to have strong impacts on SWE estimates, particularly in dense forests (Dewalle & Rango, 2008; Langlois et al., 2011). This more complex algorithm also uses the ~10 GHz channel on AMSR-E/2 and GPM, and both the vertically and horizontally polarized ~18 and ~36 GHz channels

$$SD = ff(SD_{ff}) + (1 - ff)SD_o \tag{2}$$

where ff is fractional forest cover, SD_{ff} is the SD of the forested fraction, and SD_o is the SD of the non-forested fraction. SD_{ff} and SD_o are derived with

$$SD_{ff} = p1 * (Tb_{18V} - Tb_{36V})/(1 - fd * 0.6) \tag{3}$$

$$SD_o = p1 * (Tb_{10V} - Tb_{36V}) + p2 * (Tb_{10V} - Tb_{18V}) \tag{4}$$

where fd is forest density and $p1$ and $p2$ are $1/log_{10}(Tb_{36V}\text{-}Tb_{36H})$ and $1/log_{10}(Tb_{18V}\text{-}Tb_{18H})$, respectively. While neither the MOD12Q1 nor MOD44B products cover our entire time period, we forward- and back-estimate ff and fd by linear interpolation. This has a minimal impact on intra-sensor SWE estimation, and, as forest densities are generally low across the study region, does not significantly impact our results. While attenuation of the microwave signal in forests is a large problem in many parts of the world (e.g., Northern Canada, (Foster et al., 2005)), our study region is very sparsely forested (Fig. 2D).

While both algorithms (Eqs. (1) and (2)–(4)) produce reasonable SWE estimates, previous work has shown that differences in the SSMI and AMSR-E retrieval algorithms can result in strong bias, and in particular an elevation-dependent bias (Daly et al., 2012). We present results for several single-sensor SWE time series, across multiple sensor platforms. As can be seen in Fig. 4, the *temporal patterns* of SWE are very similar across both algorithms, even if the absolute values of SWE are different. These similarities are emphasized by the black lines in Fig. 4, which are smoothed by a 21-point Savitzky-Golay filter for display purposes (Savitzky & Golay, 1964). To simplify our discussion of intra-sensor and inter-sensor SWE variabilities and the impacts of different topographic factors, we choose to use the original Chang equation (Eq. (1)) for SWE estimation, along with a constant average snow density of 0.24 g/cm ^{3} conversion factor to transform SD into SWE (Takala et al., 2011).

2.6. Understanding uncertainties in PM data

To examine possible sources of uncertainty and variance in our SWE estimates, we have divided both the SWE and raw Tb data by time of day, position along the satellite scanline, and by several topographic parameters.

2.6.1. Time of day

Previous studies (e.g., Chang et al., 1987; Chang, Foster, & Rango, 1991; Armstrong & Brodzik, 2001) have noted that night time SWE estimates are more reliable than those taken during the day, as liquid water in the snowpack drastically alters the Tb gradient used for estimating SWE. However, most studies use only one of the descending or ascending orbits, depending on the location of their study areas and hence the time of satellite overpass. We instead choose to measure solar altitude on a point-by-point basis, to ensure that all of our measured Tb values occur when the sun is below the horizon. While 90 + % of our points are derived from the descending orbits, we are also able to include some additional points from the ascending orbits during short periods of the year.

2.6.2. Scanline position

To examine the impact of satellite look angle on SWE and Tb values, we take the index position (position along the scanline) of each measured data point, and normalize it by the length of the scanline (number of captures). As each satellite captures a different swath width, and thus number of points along a scanline, this allows us to normalize our scanline positions across satellite platforms. We then subset our data into quartiles to investigate possible bias derived from satellite look angle (i.e., Quartile 1 refers to the first 25% of the scanline, cf. Fig. 5).

As can be seen in Fig. 5, Tb_{10v}, Tb_{18v}, and Tb_{36v} remain relatively constant across all scanline positions. While there are some differences between each quartile, these impacts are not consistent across the

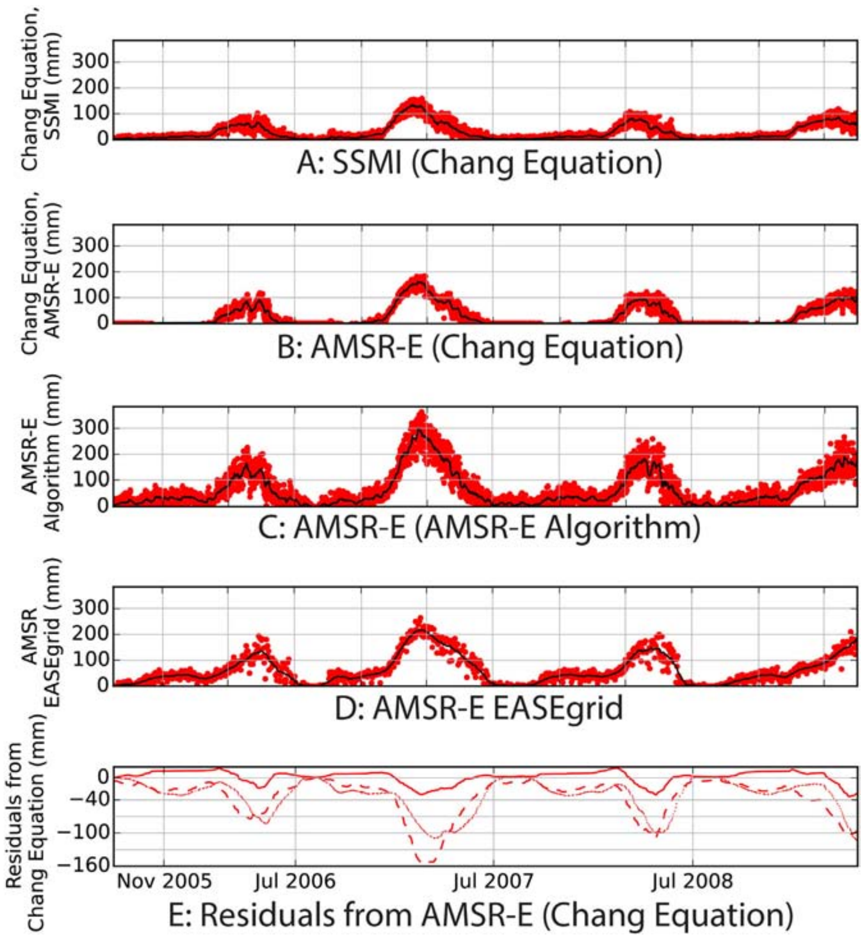

Fig. 4. Characteristic time series extracted for (76.1932°CE, 34.3335°CN, cf. Fig. 3, 2005–2009) in the NW Himalaya for the AMSR-E platform. (A) SWE based on the Chang equation (Eq. (1)) (Chang et al., 1982) in mm, data from SSMI and (B) from AMSR-E, (C) SWE based on Forest Fraction (AMSR-E) algorithm (Eq. (2)) (Kelly et al., 2003), (D) SWE based on the AMSR-E EASEgrid product (Tedesco et al., 2004). Black lines smoothed using a 21 data-point Savitzky-Golay filter (Savitzky & Golay, 1964), and used in (E) to calculate residuals of Chang equation SSMI (solid line), AMSR-E algorithm (dashed line), and AMSR EASEgrid (dotted line), with respect to the Chang equation AMSR-E SWE estimates as shown in panel (B). Time series shows generally strong agreement on the *timing* of SWE buildup and melt, but disagreements on SWE volume.

study area, and show no discernible topographic pattern. Hence, while scanline position differences throughout a single-point time series may have minor impacts upon SWE variability, these impacts are not universal or constrained across many points, and thus are not considered a major factor in influencing SWE variability.

2.7. Topography

As with forest cover, topographic parameters have long been known to impact Tb and SWE measurements (Mätzler & Standley, 2000; Armstrong & Brodzik, 2001; Mizukami & Perica, 2012; Dong et al., 2005). However, as many SWE algorithms have been calibrated over wide, flat, and forested zones (e.g., Northern Canada, Siberia), the relationship between topographic parameters and SWE estimation remains unconstrained.

Across all instruments, we see that relief and 95th percentile SWE volume are spatially correlated (Fig. 6). It is not clear whether this relationship stems from regional weather patterns, precipitation capture in complex terrain, or constructive interference in the PM spectrum over complex terrain. However, it is clear that both SWE volume and topographic parameters have impacts on SWE variability; examining whether these two impacts are manifestations of the same uncertainty in SWE measurements is outside the scope of this study.

3. Results

3.1. Linear regressions

To explore the significance of several topographic and land cover indices on SWE variability, we performed a series of linear regressions on an aggregate and by-instrument basis. For each of our 2500 randomly chosen point locations, we extracted raw PM measurements within a radius of ~10-km (0.1°), and derived measures of both bulk SWE and clear-day SWE variability (defined as days where temperature does not rise above 0 °C and there is <0.1-mm sensed precipitation) over the entire time series, which we then compare to the topographic parameters of each point (Fig. 7, Tables 2 and 3). Additional Figures and Tables for other topographic indices are available in the Supplement (Figs. S2–6, Tables S1–4).

When long-term variability in the SWE time series is compared to hillslope angle, we see significant ($p < 0.05$) results across all satellites (Table 2). When examining the entire time series, there is intrinsic variability in the SWE signal when snow falls between measurements. To control for this, we examine the SWE signal variability over only clear days. These results are also significant across all satellites, albeit with different regression slopes. This implies that hillslope angle has a direct influence on the reliability or consistency of SWE measurements, albeit with differences in regression coefficient related to PM instrument, the

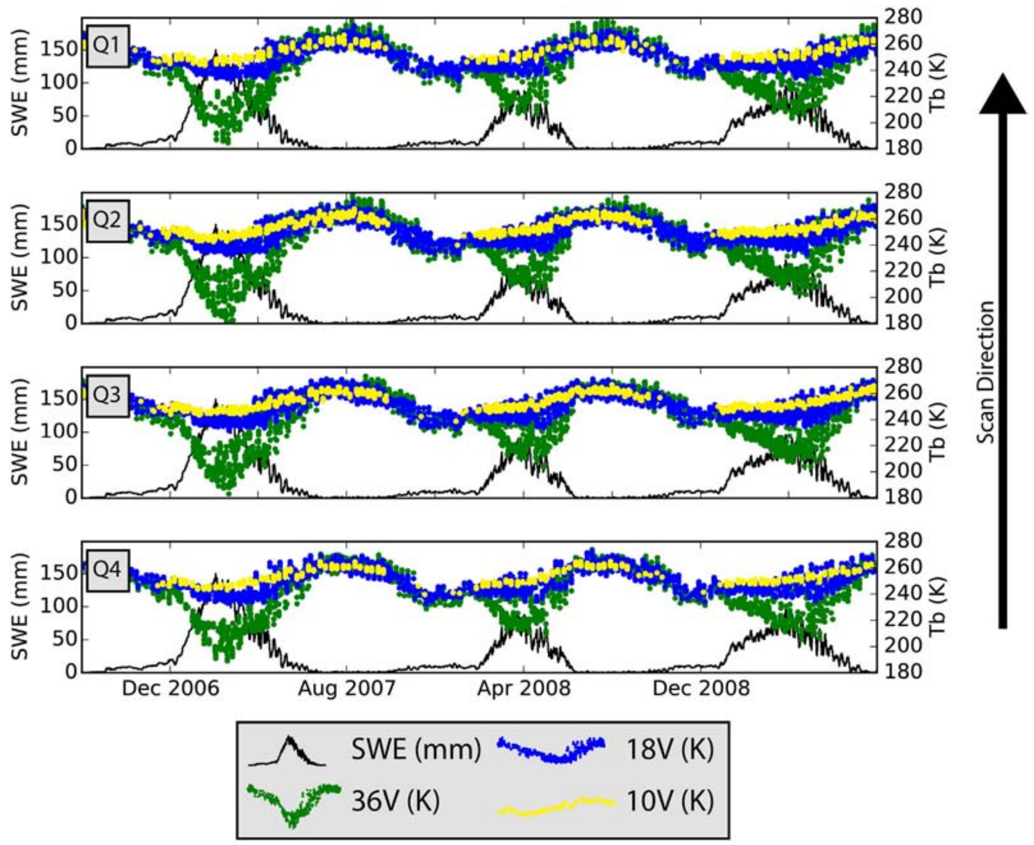

Fig. 5. Impacts of scanline position across the 10, 18, and 36 V channels for AMSR-E data (76.1932°CE, 34.3335°CN, cf. Fig. 3), divided into quartiles based on distance from satellite (black arrow indicates far to close range). SWE amount (left axis) in black, with raw 10 V (yellow), 18 V (blue), and 36 V (green) Tb values (right axis). All channels show impact of SWE buildup, with largest impacts on the 36 V channel, particularly in the spring melt periods. (For interpretation of the references to color in this figure legend, the reader is referred to the web version of this article.)

length of the sensed time series, and the temporal coverage of the time series. However, it is not clear whether the increase in SWE variability at steeper hillslopes in our study region is due solely to topographic impacts, or is also driven by regional weather patterns or other confounding effects.

Linear regressions for other topographic and land cover variables can be found in the Supplement (Tables S1–4). No other topographic indices maintain an appreciable positive or negative relationship across multiple satellites. We find, however, a significant correlation between clear-day SWE variation and long-term wind patterns, as measured by HAR 10-m wind speed (Table 3).

For mean, median, 25th, 75th, and 90th percentile long-term DJF wind speeds, we see significant relationships, where consistently low-wind areas (low 25th percentile wind speeds) exhibit higher variance in SWE estimates (additional regression results available in the Supplement, Tables S1–4). There are significant differences in the regression slopes across different satellite platforms, in both Tables 2 and 3. We attribute this to differences in data capture time, data density, and the temporal range of the different satellite platforms. These differences indicate that any blended or multi-instrument SWE product must account for these differences to generate an accurate SWE estimate.

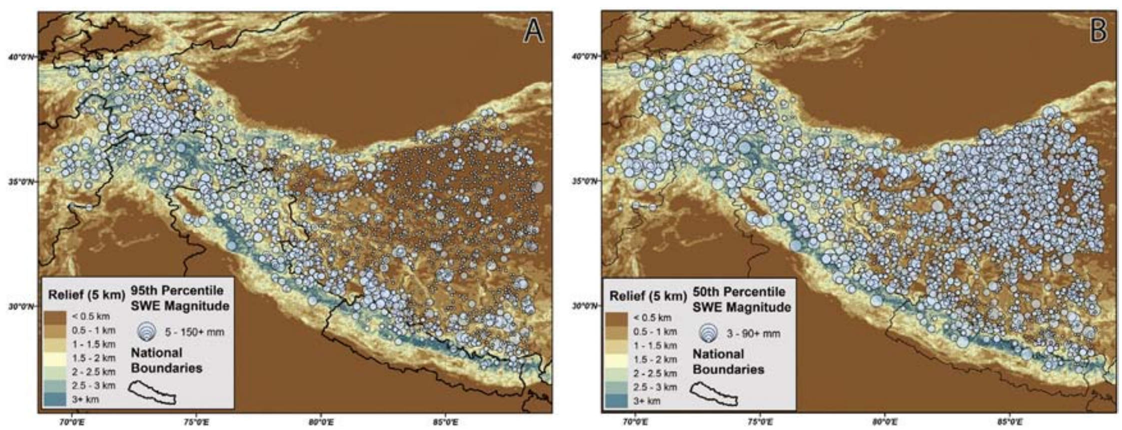

Fig. 6. (A) Multi-year maximal SWE, proxied by 95th percentile SWE volume, and (B) 50th percentile SWE volume, over the period 2000–2015, calculated from a merged dataset of daily values across all sensors. 5-km radius topographic relief in background.

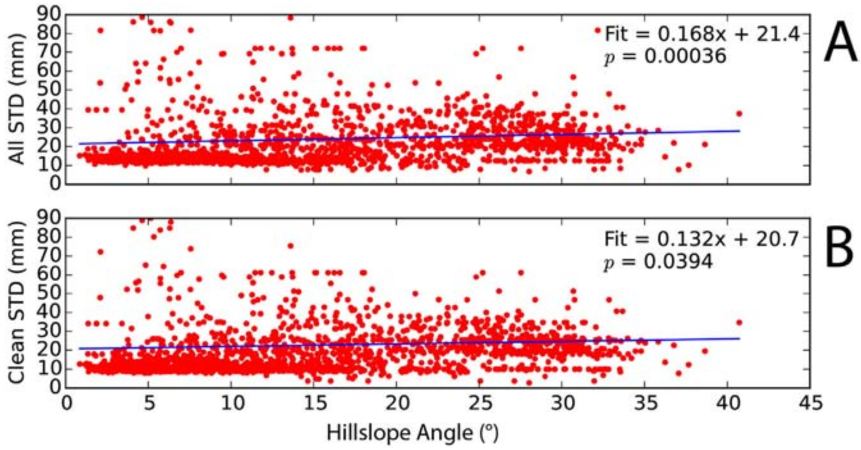

Fig. 7. Correlation between SWE variability (standard deviation, STD) and hillslope angle across all instruments and all sample points show in Fig. 1 (n = 2500). (A) Aggregate total variability on y-axis and (B) clear-day variability on the y-axis, with regression lines and p-values on each. Individual regression results available in Table 2.

4. Discussion

4.1. Multiple regression

To determine the relative impacts of several variables on clear-day SWE variability, we set up a multiple regression, with clear-day SWE standard deviation as the independent variable and maximal SWE volume, forest fraction, hillslope angle, relief, elevation and both 25th and 90th percentile DJF wind speeds as dependent variables. In this analysis, we use 95th percentile SWE volume, calculated over the entire time series, as a proxy for maximal SWE volume (Table 4). While SWE variation within a single PM footprint is likely to influence SWE variability, without significant in-situ data these impacts are hard to quantify. In this regression, we assume that some of the in-footprint variability is proxied by both topographic relief and by wind speeds, which could both impact the distribution of SWE within a single PM pixel.

We observe that forest fraction is the strongest control on SWE variability (Table 4). This is followed by long-term 95th percentile SWE, 90th percentile DJF wind speed, 25th percentile DJF wind speed, hillslope angle, relief, and elevation. Interestingly, terrain slope has a ~10 times greater effect upon SWE variability than terrain relief does in our study area (Table 4).

In our study region, there are relatively few geographic areas with significant forest cover (cf. Fig. 2D). When a multiple regression is performed only on points with <5% forest fraction (the majority of our study area), the coefficients of regression for each of the other variables are nearly identical, as can be seen in Table S6 of the Supplement. This implies that forest fraction has very little impact upon the relationship between SWE variability and the other variables used in the multiple regression in HMA. We do not have enough sample points with dense forest cover to provide statistically significant results for a similar regression analysis on only those points with >5% forest fraction.

While forest fraction is a factor controlled for in modern SWE estimation algorithms, wind speed, topographic slope, and maximal SWE volume are not. These factors will all have impacts on SWE estimation, and can help account for some of the uncertainty noted in SWE estimation studies (e.g., Mizukami & Perica, 2012; Dai et al., 2015; Foster et al., 2005; Tedesco & Narvekar, 2010). In particular, the sensitivity of SWE variance to 95th percentile SWE implies that deep snow is still very difficult for PM SWE algorithms to estimate. Several studies have noted that SWE estimation becomes far less reliable when SWE is >200-mm (e.g. Vuyovich, Jacobs, & Daly, 2014; Clifford, 2010; Andreadis & Lettenmaier, 2006; Tong et al., 2010; Dong et al., 2005). While both the Tb_{10v} and Tb_{18v} signals will be impacted by snow surface temperatures, several authors note that the Tb_{10v} signal is less influenced by deep snowpack than the Tb_{18v} (e.g., Kelly, 2009; Derksen, 2008; Tedesco et al., 2015; Tong et al., 2010).

This effect is particularly pronounced in regions where there is constant or nearly-constant snow cover (e.g., Fig. 8). Throughout the year, and in particular during the winter months, all three channels (Tb_{10v}, Tb_{18v}, and Tb_{36v}) are impacted by snow buildup, even though the Tb_{10v} and Tb_{18v} channels are treated as a 'bare-soil' signal by many algorithms (e.g., Chang et al., 1987; Kelly et al., 2003; Pulliainen, 2006; Kelly, 2009; Takala et al., 2011; Mizukami & Perica, 2012; Savoie et al., 2009; Derksen, 2008). This snow signal is captured by both the Chang equation (Fig. 8B2) and the AMSR-E SWE algorithm (Fig. 8B3), although it is unlikely that either estimate properly captures the *magnitude* of SWE. It is likely that those areas which see constant or nearly-constant snow cover develop larger snow crystals, which interfere more strongly with the Tb_{10v} and Tb_{18v} channels than fresh or seasonal snow. However, without in-situ data, it is difficult to separate these two interacting impacts.

While some point locations in our dataset see constant snow cover (cf. Fig. 8), this effect is also visible in areas with seasonal snow cover

Table 2
Slopes of regressions against hillslope angle (n = 2500), including p-values, t-values, and 95% confidence intervals (CI). Total individual points (all days/clear-day): All Satellites (30,865,102/14,804,414), SSMI (2,224,350/1,586,970), SSMIS (4,089,875/2,786,589), AMSR-E (15,302,564/7,284,209), AMSR2 (6,660,429/2,678,470), GPM (2,587,848/468,176).

Metric	All satellites	SSMI	SSMI/S	AMSR-E	AMSR2	GPM
All-day slope	0.168	0.491	0.359	0.17	0.45	0.322
All-day slope p-values	**0.00036**	**2.92e-109**	**4.5e-69**	**0.0261**	**4.63e-55**	**1.42e-28**
All-day slope t-values	3.57	23.4	18.1	2.23	16	11.2
All-day slope CI	0.0905–0.245	0.457–0.526	0.327–0.392	0.0443–0.296	0.404–0.296	0.274–0.369
Clean-day slope	0.311	0.141	0.463	6.64	0.458	0.109
Clean-day slope p-values	**5.43e-07**	**0.031**	**1.94e-108**	**9.83e-91**	9**.74e-75**	**1.42e-28**
Clean-day slope t-values	5.02	2.16	23.3	21.1	18.9	1.24
Clean-day slope CI	0.209–0.412	0.0334–0.248	0.43–0.495	6.12–7.16	0.418–7.16	−0.0352–0.252

Bold values indicate statistically significant results ($p < 0.05$).

Table 3
Slopes of regressions against 14-year 25th percentile 10-m DJF Wind Speed (n = 2500), including *p*-values, *t*-values, and 95% confidence intervals (CI). Total individual points (all days/clear-day): All Satellites (30,865,102/14,804,414), SSMI (2,224,350/1,586,970), SSMIS (4,089,875/2,786,589), AMSR-E (15,302,564/7,284,209), AMSR2 (6,660,429/2,678,470), GPM (2,587,848/468,176).

Metric	All satellites	SSMI	SSMI/S	AMSR-E	AMSR2	GPM
All-day slope	−1.27	−0.28	−0.565	−1.37	−0.525	−1.11
All-day slope *p*-values	**1.57e-06**	**0.0327**	**2.03e-06**	**0.00146**	**0.00161**	**1.54e-11**
All-day slope *t*-values	−4.81	−2.14	−4.76	−3.19	−3.16	−6.78
All-day slope CI	−1.71 to −0.838	−0.495 to −0.0643	−0.76 to −0.37	−2.08 to −0.662	−0.798 to −0.662	−1.38 to −0.842
Clean-day slope	−1.12	−1.57	−0.306	13.9	−0.693	−1.64
Clean-day slope *p*-values	**0.00143**	**7.29e-06**	**0.013**	**5.86e-100**	**3.64e-06**	**1.54e-11**
Clean-day slope *t*-values	−3.19	−4.49	−2.48	22.2	−4.64	−2.86
Clean-day slope CI	−1.69 to −0.541	−2.14 to −0.995	−0.508 to −0.103	12.9–15	−0.939-15	−2.59 to −0.696

Bold values indicate statistically significant results ($p < 0.05$).

(cf. Fig. 5). Those points with constant deep snow cover are likely to *weaken* the relationship between maximal SWE depth and SWE variability by lowering the possible range of SWE values. Despite the potential for SWE signal saturation at high snow depths, we still see a strong positive correlation between 95th percentile SWE and SWE variability.

Both 90th and 25th percentile DJF 10-m wind speeds show strong impacts in our multiple regression. We attribute this effect – which is not consistent across all satellites – to wind-blown snow redistribution. Areas of high wind are typically topographically complex, and see wind-blown snow redistribution mostly in the form of avalanches which do not travel much further than the extent of a single PM pixel. These regions typically see more annual snow as well, which could confound the wind signal. However, low-wind areas, which correlate with large, flat regions in our study area, could see snow redistribution over a very large area, especially if there are few windbreaks.

4.2. Spatial distribution of uncertainties

Based on our multiple-regression analysis, we have developed a map showing the distribution of SWE uncertainty throughout our study area (Fig. 9). This is based on topographic parameters, HAR wind speed, land cover (MOD12Q1), and long-term 95th percentile SWE estimates derived from daily AMSR-E EASEgrid SWE measurements (2002−2011) (Tedesco et al., 2004), and does not include any uncertainties introduced by differing algorithms or 'instantaneous' ground conditions, such as precipitation or snow recrystallization. We use the AMSR-E EASEgrid to generate our SWE volume proxy as it covers the whole study area with a continuous surface at a comparable spatial resolution to the other input datasets.

As can be seen in Fig. 9, SWE uncertainty is strongly correlated with complex topography, as has been proposed in previous publications (Mizukami & Perica, 2012; Tedesco & Narvekar, 2010). However, the multiple regression also implies that topographic complexity is not the only controlling variable. For example, the north-central portions of the Tibetan Plateau, while topographically flat, see relatively high SWE variation due to the combination of higher snowfall totals than the south-eastern areas of the Plateau and more wind-related snow redistribution. These estimates can provide a first-order assessment of SWE measurement reliability throughout the world, and particularly in regions where ground-truth data is sparse. While a generalized uncertainty map combining the results of all of the satellite time series would be desirable, the multiple regression results on a by-satellite basis (available in the Supplement, Tables S5–16) indicate that there are important differences in regression coefficients across satellites. When considered in aggregate, these differences dilute the uncertainty signatures of each individual satellite. As each satellite responds slightly differently to topographic, land cover, and climatic factors, in both positive and negative directions, the aggregate regression encompasses a wider spread of uncertainties, and thus shows the least significant correlations (see Supplement, Figs. S10–15 and Tables S5–16). The different responses of each satellite are likely due to differences in spatial, temporal, and spectral resolution and instrument hardware.

Despite these differences in uncertainty, all five satellites are able to track the *patterns* of SWE over our multi-year time series (cf. Fig. 10). The largest differences between SWE amounts on an annual basis come when SWE amounts are greatest – for example in 2007 and 2010 – and when the SWE time series does not encompass the entire 3-month DJF period – for example in 2002 (cf. Fig. 10).

In our analysis, spectral resolution has the least influence on differences in SWE volume uncertainty across satellite platforms, as we use only two bands (Tb_{18v} and Tb_{36v}) in our calculations of SWE. These bands are present across all satellites, albeit with slight differences in exact channel frequency (Table 1). These channel differences are controlled for in the application of the Chang Equation (Eq. (1)), after (Armstrong & Brodzik, 2001). Differences in the temporal range and resolution of each satellite dataset could influence our calculated uncertainties, particularly due to differences in snow cover during multiple winter periods. For example, AMSR-E (2002–2011) has several different winters of data, while GPM (2014–2015) only has data from a single complete winter. However, there is high variation in both the regression coefficients and *p*-values when the multiple regressions are performed on a year-by-year basis. The coefficients tend to oscillate around a multi-year norm, indicating that while the multi-year regressions provide the long-term mean coefficients, the highest significance uncertainty signal will come from those data with a shorter observation period, such as GPM.

As the spatial resolutions of GPM and AMSR-E/2 are higher than those of SSMI/S (e.g., Fig. 3), there is less intrinsic terrain variability in a single GPM/AMSR pixel than in a single SSMI/S pixel. This implies that, all other factors being equal, the SWE estimates from GPM and

Table 4
Coefficients of Multiple Regressions for GPM (n = 2500), including *p*-values, *t*-values, 95% confidence intervals (CI), and percentage of total variance.

Metric	Coefficient	*p*-value	*t*-value	Confidence interval	Percent of total
Forest Fraction	2.97	0.206	1.27	−1.63–7.57	75.8%
95th Percentile SWE	0.306	**0**	206	0.303–0.309	7.82%
90th Percentile Wind	0.22	**2.13e-08**	5.62	0.143–0.297	5.62%
25th Percentile Wind	−0.213	**0.000953**	−3.31	−0.34 to −0.087	5.44%
Hillslope Angle	0.205	**6.84e-23**	9.95	0.165–0.246	5.24%
Relief	−0.00236	**9.93e-17**	−8.36	−0.003 to −0.002	0.0603%
Elevation	−0.00224	**4.86e-317**	−44.4	−0.002 to −0.002	0.0572%

Bold values indicate statistically significant results ($p < 0.05$).

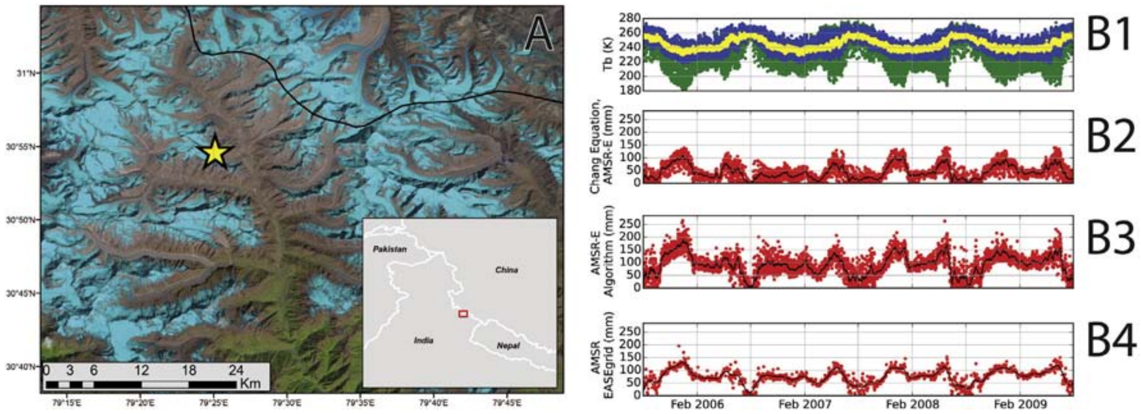

Fig. 8. (A) Landsat 8 Image (Oct 5, 2015, LC81450392015276LGN00), showing a point location in the western Himalaya (79.418247, 30.911184) surrounded by glaciers. (B1) Raw 10 V (yellow), 18 V (blue), and 37 V (green) signal; (B2) Chang equation SWE estimates, with AMSR-E data; (B3) AMSR-E algorithm SWE estimates; (B4) AMSR EASEgrid SWE estimates. Illustrates how persistent snow cover can disrupt the 10 V signal. SWE is also likely significantly underestimated in locations such as this with glacial ice or deep snow cover.

AMSR-E/2 will be of a higher quality (cf. Fig. 9, and Figs. S10–15 in the Supplement). As these sensors also gather additional spectral frequencies, they are also suitable for more complicated SWE algorithms, such as those shown in Eqs. (2)–(4).

4.3. Discussion of additional SWE uncertainties

The above regressions have noted some possible topographic, land cover, and weather-related SWE measurement uncertainty sources. However, there are several other possible uncertainty sources, which have been accounted for to varying degrees in previous work.

The first possible source of uncertainty, which is difficult to control for, is inter- and intra-sensor biases. Some studies, such as (Dai et al., 2015), have identified SWE biases between the various satellites of the SSMI/S constellation. Intercalibration of multiple satellites is challenging due to the dearth of wide-scale and long-term SWE ground measurements. Additionally, the Tb_{18v} channel present on all of the studied satellites is considered as a clean soil signal from the snow-covered earth in the Chang equation. However, the influence of SWE buildup can be seen clearly in this channel, for example in Figs. 5 and 8. While modern algorithms also take advantage of the Tb_{10v} signal for deep-snow estimation (e.g., Kelly, 2009; Tedesco & Narvekar, 2010; Derksen, 2008), Fig. 8 also shows SWE influence on that channel. Therefore, there will be inherent bias in any SWE estimation, especially in deep-snow situations.

Previous work has also implicated high relief areas as low SWE confidence areas (Mätzler & Standley, 2000; Tedesco & Narvekar, 2010). This is due to relief not only influencing the size of the satellite footprint through shadowing, but also changing the relative satellite look angle and angle of incidence for polarization. Our results indicate that topographic parameters do indeed influence SWE reliability, although it is not clear whether overshadowing, satellite look angle, polarization changes, or a secondary impact of topography such as precipitation capture are most responsible for changes in SWE reliability. Additionally, terrain slope has a much larger impact upon SWE variability than terrain relief does in our study area (Table 4).

5. Conclusion

This study presents a multi-parameter uncertainty assessment of passive microwave (PM) snow-water equivalent (SWE) estimation using the Special Sensor Microwave/Imager (SSMI), Special Sensor Microwave Imager/Sounder (SSMIS), Advanced Microwave Scanning Radiometer - Earth Observing System (AMSR-E), AMSR2, and Global Precipitation Measurement (GPM) satellites. We identify and assess a suite of possible uncertainty sources in the raw PM data, as well as in the SWE estimations from multiple overlapping time series. We use

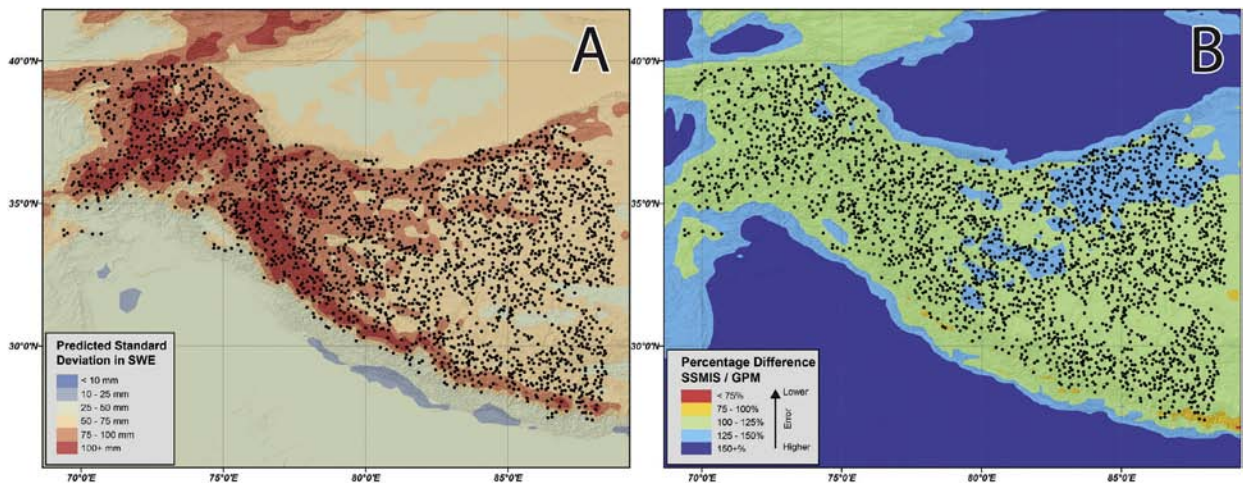

Fig. 9. Spatial distribution showing SWE uncertainties from PM data using (A) the multi-parameter estimated using regression coefficients from the GPM satellite (one year of data, Table 4). (B) Percentage difference between the uncertainty of the SSMIS satellite and the uncertainty of the GPM satellite (100% indicates equal uncertainty in both satellites, lower values indicate SSMIS is better) and black arrow in the legend indicates direction from high to low uncertainty. In general, the GPM satellite shows lower uncertainty across the entire study area. Additional comparisons available in the Supplement (Figs. S10–15).

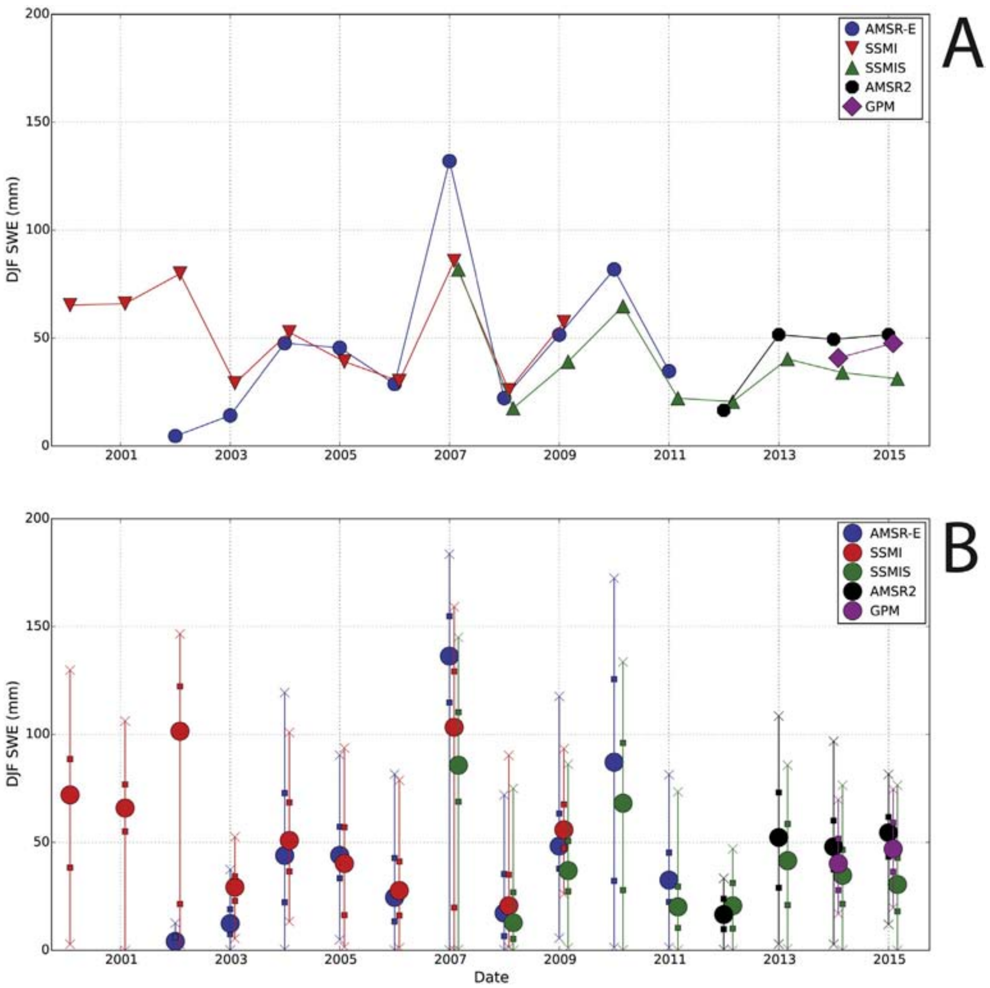

Fig. 10. (A) Annual DJF mean SWE amounts at a single point (cf. Fig. 3), as sensed by SSMI (red), AMSR-E (blue), SSMIS (green), AMSR2 (black), and GPM (magenta). (B) Annual DJF median SWE amounts with DJF minima and maxima (Xs) and first and third quartiles (squares) for each. Illustrates that while each instrument senses slightly different SWE *amounts*, the inter-annual patterns of SWE are consistent across the satellites. (For interpretation of the references to color in this figure legend, the reader is referred to the web version of this article.)

these uncertainty sources to develop a multi-parameter estimation of inherent unreliability in SWE estimates across High Mountain Asia, including the Tibetan Plateau and the Himalaya. We find that forest fraction is the strongest control on SWE variability, followed by long-term maximal SWE volume, wind speed, and hillslope angle. Elevation, relief, and terrain aspect show very low influence on SWE variability. While forest cover and topographic parameters have been integrated into many SWE algorithms, wind speed and long-term maximal SWE volume have not. The results derived here show that wind-redistribution of snow can have impacts on SWE, especially over large, flat, areas. The uncertainty map developed here provides a first-order approximation of SWE-estimate reliability for much of High Asia, and implies that high-fidelity SWE estimates can be produced for a range of elevation zones and terrain types. We find that each individual satellite shows differences in SWE variability, with the more modern sensors (GPM, AMSR-E/2) providing the most robust SWE estimates, expressed in this analysis as low SWE variability.

Appendix A. Supplementary data

Supplementary data to this article can be found online at http://dx.doi.org/10.1016/j.rse.2016.03.037.

References

Anderton, S., White, S., & Alvera, B. (2002). Micro-scale spatial variability and the timing of snow melt runoff in a high mountain catchment. *Journal of Hydrology*, *268*, 158–176.

Andreadis, K. M., & Lettenmaier, D. P. (2006). Assimilating remotely sensed snow observations into a macroscale hydrology model. *Advances in Water Resources*, *29*, 872–886.

Armstrong, R., & Brodzik, M. (2001). Recent Northern Hemisphere snow extent: A comparison of data derived from visible and microwave satellite sensors. *Geophysical Research Letters*, *28*, 3673–3676.

Armstrong, R. L., & Brodzik, M. J. (2002). Hemispheric-scale comparison and evaluation of passive-microwave snow algorithms. *Annals of Glaciology*, *34*, 38–44.

Ashcroft, P., & Wentz, F. (2013). *AMSR-E/aqua L2A global swath spatially-resampled brightness temperatures V003, [2002 −2010]*. National Snow and Ice Data Center: Boulder, Colorado USA.

Bookhagen, B., & Burbank, D. W. (2010). Toward a complete Himalayan hydrological budget: Spatiotemporal distribution of snowmelt and rainfall and their impact on river discharge. *Journal of Geophysical Research: Earth Surface*, *115* (2003–2012).

Brown, R. (1996). Evaluation of methods for climatological reconstruction of snow depth and snow cover duration at Canadian meteorological stations. *Proc. Eastern Snow Conf., 53d Annual mMeeting* (pp. 55–65).

Chang, A., Foster, J., & Hall, D. (1987). Nimbus-7 SMMR derived global snow cover parameters. *Annals of Glaciology*, *9*, 39–44.

Chang, A., Foster, J., & Hall, D. (1996). Effects of forest on the snow parameters derived from microwave measurements during the BOREAS winter field campaign. *Hydrological Processes*, *10*, 1565–1574.

Chang, A., Foster, J., Hall, D., Rango, A., & Hartline, B. (1982). Snow water equivalent estimation by microwave radiometry. *Cold Regions Science and Technology*, *5*, 259–267.

Chang, A., Foster, J., & Rango, A. (1991). Utilization of surface cover composition to improve the microwave determination of snow water equivalent in a mountain basin. *Remote Sensing*, *12*, 2311–2319.
Clifford, D. (2010). Global estimates of snow water equivalent from passive microwave instruments: History, challenges and future developments. *International Journal of Remote Sensing*, *31*, 3707–3726.
Dai, L., Che, T., & Ding, Y. (2015). Inter-calibrating SMMR, SSM/I and SSMI/S data to improve the consistency of snow-depth products in China. *Remote Sensing*, *7*, 7212–7230.
Daly, S. F., Vuyovich, C. M., Deeb, E. J., Newman, S. D., Baldwin, T. B., & Gagnon, J. J. (2012). Assessment of the snow conditions in the major watersheds of Afghanistan using multispectral and passive microwave remote sensing. *Hydrological Processes*, *26*, 2631–2642.
Derksen, C. (2008). The contribution of AMSR-E 18.7 and 10.7 GHz measurements to improved boreal forest snow water equivalent retrievals. *Remote Sensing of Environment*, *112*, 2701–2710.
Dewalle, D. -P., & Rango, A. (2008). *Snowpack energy exchange: Topographic and forest effects.*
DiMiceli, C., Carroll, M., Sohlberg, R., Huang, C., Hansen, M., & Townshend, J. (2011). *Annual global automated MODIS vegetation continuous fields (MOD44B) at 250 m spatial resolution for data years beginning day 65, 2000–2010, collection 5 percent tree cover.* USA: University of Maryland, College Park, MD.
Dong, J., Walker, J. P., & Houser, P. R. (2005). Factors affecting remotely sensed snow water equivalent uncertainty. *Remote Sensing of Environment*, *97*, 68–82.
Dozier, J., & Warren, S. G. (1982). Effect of viewing angle on the infrared brightness temperature of snow. *Water Resources Research*, *18*, 1424–1434. http://dx.doi.org/10.1029/WR018i005p01424.
Dozier, J., Painter, T. H., Rittger, K., & Frew, J. E. (2008). Time–space continuity of daily maps of fractional snow cover and albedo from MODIS. *Advances in Water Resources*, *31*, 1515–1526.
Foster, J. L., Sun, C., Walker, J. P., Kelly, R., Chang, A., Dong, J., & Powell, H. (2005). Quantifying the uncertainty in passive microwave snow water equivalent observations. *Remote Sensing of Environment*, *94*, 187–203.
GPM Science Team (2014). *GPM GMI level 1B brightness temperatures, version 03, greenbelt.* MD, USA: NASA Goddard Earth Science Data and Information Services Center (GES DISC).
Guan, B., Molotch, N. P., Waliser, D. E., Jepsen, S. M., Painter, T. H., & Dozier, J. (2013). Snow water equivalent in the Sierra Nevada: Blending snow sensor observations with snowmelt model simulations. *Water Resources Research*, *49*, 5029–5046.
Hansen, M., DeFries, R., Townshend, J., Carroll, M., Dimiceli, C., & Sohlberg, R. (2003). Global percent tree cover at a spatial resolution of 500 meters: First results of the MODIS vegetation continuous fields algorithm. *Earth Interactions*, *7*, 1–15.
Huffman, G. J., Bolvin, D. T., Nelkin, E. J., Wolff, D. B., Adler, R. F., Gu, G., ... Stocker, E. F. (2007). The TRMM multisatellite precipitation analysis (TMPA): Quasi-global, multiyear, combined-sensor precipitation estimates at fine scales. *Journal of Hydrometeorology*, *8*, 38–55.
Imaoka, K., Kachi, M., Kasahara, M., Ito, N., Nakagawa, K., & Oki, T. (2010). Instrument performance and calibration of AMSR-E and AMSR2, international archives of the photogrammetry. *Remote Sensing and Spatial Information Science*, *38*, 13–18.
Immerzeel, W. W., Droogers, P., De Jong, S., & Bierkens, M. (2009). Large-scale monitoring of snow cover and runoff simulation in Himalayan river basins using remote sensing. *Remote Sensing of Environment*, *113*, 40–49.
Jarvis, A., Reuter, H. I., Nelson, A., Guevara, E., et al. (2008). Hole-filled SRTM for the globe version 4. available from the CGIAR-CSI SRTM 90m Database http://srtm.csi.cgiar.org
Kelly, R. (2009). *The AMSR-E snow depth algorithm: Description and initial results Vol. 29. (pp. 307–317), 307–317.*
Kelly, R. E., Chang, A. T., Tsang, L., & Foster, J. L. (2003). A prototype AMSR-E global snow area and snow depth algorithm. *IEEE Transactions on Geoscience and Remote Sensing*, *41*, 230–242.
Knowles, K., Njoku, E., Armstrong, R., & Brodzik, M. J. (2002). *Nimbus-7 SMMR pathfinder daily EASE-grid brightness temperatures.* Digital Media.
Langlois, A., Royer, A., Dupont, F., Roy, A., Gota, K., & Picard, G. (2011). Improved corrections of forest effects on passive microwave satellite remote sensing of snow over boreal and subarctic regions. *IEEE Transactions on Geoscience and Remote Sensing*, *49*, 3824–3837.
Mätzler, C., & Standley, A. (2000). Technical note: Relief effects for passive microwave remote sensing. *International Journal of Remote Sensing*, *21*, 2403–2412.
Maussion, F., Scherer, D., Mölg, T., Collier, E., Curio, J., & Finkelnburg, R. (2014). Precipitation seasonality and variability over the Tibetan Plateau as resolved by the High Asia Reanalysis*. *Journal of Climate*, *27*, 1910–1927.
Mizukami, N., & Perica, S. (2012). Towards improved snow water equivalent retrieval algorithms for satellite passive microwave data over the mountainous basins of western USA. *Hydrological Processes*, *26*, 1991–2002.
Molotch, N. P., & Margulis, S. A. (2008). Estimating the distribution of snow water equivalent using remotely sensed snow cover data and a spatially distributed snowmelt model: A multi-resolution, multi-sensor comparison. *Advances in Water Resources*, *31*, 1503–1514.
Painter, T. H., Rittger, K., McKenzie, C., Slaughter, P., Davis, R. E., & Dozier, J. (2009). Retrieval of subpixel snow covered area, grain size, and albedo from MODIS. *Remote Sensing of Environment*, *113*, 868–879.
Pulliainen, J. (2006). Mapping of snow water equivalent and snow depth in boreal and sub-arctic zones by assimilating space-borne microwave radiometer data and ground-based observations. *Remote Sensing of Environment*, *101*, 257–269.
Savitzky, A., & Golay, M. J. (1964). Smoothing and differentiation of data by simplified least squares procedures. *Analytical Chemistry*, *36*, 1627–1639.
Savoie, M. H., Armstrong, R. L., Brodzik, M. J., & Wang, J. R. (2009). Atmospheric corrections for improved satellite passive microwave snow cover retrievals over the Tibet Plateau. *Remote Sensing of Environment*, *113*, 2661–2669.
Sun, N., & Weng, F. (2008). Evaluation of special sensor microwave imager/sounder (SSMIS) environmental data records. *IEEE Transactions on Geoscience and Remote Sensing*, *46*, 1006–1016.
Takala, M., Luojus, K., Pulliainen, J., Derksen, C., Lemmetyinen, J., Kärnä, J. -P., ... Bojkov, B. (2011). Estimating northern hemisphere snow water equivalent for climate research through assimilation of space-borne radiometer data and ground-based measurements. *Remote Sensing of Environment*, *115*, 3517–3529.
Takala, M., Pulliainen, J., Metsämäki, S. J., & Koskinen, J. T. (2009). Detection of snowmelt using spaceborne microwave radiometer data in Eurasia from 1979 to 2007. *IEEE Transactions on Geoscience and Remote Sensing*, *47*, 2996–3007.
Tedesco, M., & Narvekar, P. S. (2010). Assessment of the NASA AMSR-E SWE product. *IEEE Journal of Selected Topics in Applied Earth Observations and Remote Sensing*, *3*, 141–159.
Tedesco, M., Derksen, C., Deems, J. S., & Foster, J. L. (2015). Remote sensing of snow depth and snow water equivalent. *Remote sensing of the cryosphere* (pp. 73–98).
Tedesco, M., Kelly, R., Foster, J. L., & Chang, A. T. (2004). *AMSR-E/aqua daily L3 global snow water equivalent EASE-grids. Version 2. 2002–2011.* Boulder, Colorado USA: NASA National Snow and Ice Data Center Distributed Active Archive Center.
Tong, J., Dery, S. J., Jackson, P. L., & Derksen, C. (2010). Testing snow water equivalent retrieval algorithms for passive microwave remote sensing in an alpine watershed of western Canada. *Canadian Journal of Remote Sensing*, *36*, S74–S86.
Vander Jagt, B. J., Durand, M. T., Margulis, S. A., Kim, E. J., & Molotch, N. P. (2013). The effect of spatial variability on the sensitivity of passive microwave measurements to snow water equivalent. *Remote Sensing of Environment*, *136*, 163–179.
Vuyovich, C. M., Jacobs, J. M., & Daly, S. F. (2014). Comparison of passive microwave and modeled estimates of total watershed SWE in the continental United States. *Water Resources Research*, *50*, 9088–9102.
Wang, J., & Tedesco, M. (2007). Identification of atmospheric influences on the estimation of snow water equivalent from AMSR-E measurements. *Remote Sensing of Environment*, *111*, 398–408.
Wentz, F. J. (2013). SSM/I version-7 calibration report. *Remote Sensing Systems Report*, *11012*, 46.